

# Radiation Force of Gaussian Beam on Spherical Particle with Fourier Transform, Lorenz-Mie Theory and Maxwell Stress Tensor

Chou-Wei Kiang and Jean-Fu Kiang

**Abstract**—An FT-LMT-MST approach is proposed to compute the radiation force exerted by a Gaussian beam on a spherical particle, by integrating the Fourier transform method, the Lorenz-Mie theory and the Maxwell stress tensor. A rigorous formulation is derived and implemented for numerical simulations. Distributions of electric field and radiation force density are analyzed. The phenomena of negative force density and oscillation of radiation force versus particle size are discussed.

## I. INTRODUCTION

Radiation force exerted by laser has found versatile applications in manipulating particles of micrometer and nanometer scales [1]. Since Ashkin and his coworkers published several articles in the 1970s, regarding laser radiation force in accelerating, trapping [2] and optical levitating [3] of particles, the radiation force at radio frequency [4] and optical frequency [3], [5] has been widely studied.

Radiation force has been used for remote manipulation of particles via laser trapping and laser guidance [1]. To perform laser trapping, large numerical aperture ( $NA > 1$ ) is required to maintain a highly convergent beam, inducing reverse radiation pressure to trap particles within a few micrometers of the focal point. Laser guidance demands a smaller numerical aperture ( $NA \sim 0.1$ ) to form a mildly convergent beam. The particles can be transported over a distance of tens to hundreds times of particle radius.

The radiation force has also been exploited in microfluid/nanofluid systems for biological, clinical and environmental applications [6]. Optical tweezers are useful tools for manipulating single biological cell in biological and biomedical researches [7]. A highly-focused laser beam is typically used in optical tweezers, inducing non-uniform fields near the target cell to manipulate it [7].

The intensity of radiation force is determined by the properties of particle, the background medium and the characteristics (magnitude, phase, frequency) of the wave field [6]. Analytical and computational methods have been used to study the radiation force for decades. The radiation force can be characterized by the relative dimensions between laser wavelength and particle size [5]. In the Rayleigh scattering regime, the particle size is smaller than one wavelength, the dipole approximation is valid and the magnetic fields can be neglected [4], [5]. In

the ray-optics regime, the particle size is much larger than one wavelength, ray-optics methods like geometrical optics can be applied to compute the radiation force via multiple reflections and refractions [5].

Between ray-optics and Rayleigh scattering regimes, the Lorenz-Mie theory (LMT) provides a closed-form solution of electric and magnetic fields with a plane wave incident upon a spherical particle [8], based on which the radiation force can be determined [1], [5], [9]. Practical light sources are often modeled as Gaussian beams, various theories and simulation models on radiation force exerted by a Gaussian beam have been proposed [1], [10], [11], [12]. In [10], a generalized Lorenz-Mie theory (GLMT) was proposed to solve a scattering problem with an on-axis Gaussian beam incident upon a spherical particle. A localization approximation based on the van de Hulst's localization principle was used to calculate the beam-shape coefficients of the Gaussian beam. The localization approximation was constrained by the Rayleigh-Gans theory, and was valid if the refractive indices of particle and background medium were close. In [12], a Bromwich formulation in curvilinear coordinates was used to derive the scattering theory of a Gaussian beam incident upon a spherical particle.

In [11], the electric and magnetic fields in spherical coordinates were given in terms of Ricatti-Bessel functions and spherical harmonics. The net radiation force and torque exerted by a monochromatic incident beam were derived from a Maxwell stress tensor (MST), but the fields and force distributions on the particle surface were not elaborated. The Maxwell stress tensor was derived from the balance of electromagnetic momentum, and the radiation force was derived from the interaction between the charge and current distributions within the particle and the external electromagnetic fields [13]. The total fields exterior to the particle were composed of incident fields and Mie scattering fields [9], [14]. Maxwell stress tensor has been used to compute the normal radiation pressure and tangential radiation stress on the surface of a dielectric particle induced by external electromagnetic fields [15]. In [9], Maxwell stress tensor and Lorentz force were applied to determine the radiation force exerted by a uniform plane wave (UPW) incident upon a two-dimensional dielectric or magnetic particle. Oscillation or resonance phenomenon was observed in the curve of radiation pressure versus particle radius, for dielectric and magnetic particles, slabs and cylinders, which became more distinct as the particle size increases [9].

A Gaussian beam can be decomposed into a continuous

spectrum of plane waves, in the form of Fourier transform (FT) [16], [17]. In [16], an incident Gaussian beam was Fourier transformed to determine the fields interior to a spherical particle, expressed in terms of spherical vector wave functions. A Gaussian beam can be shaped via modulating the Fourier transform of the input to a Fourier optics lens system [17]. However, Fourier transform has not been used in computing the radiation force exerted by a Gaussian beam on a spherical particle.

In this work, we propose an FT-LMT-MST approach by applying Fourier transform (FT), Lorenz-Mie theory (LMT) and Maxwell stress tensor (MST) to compute the radiation force of a Gaussian beam (GB) exerted on a spherical particle. The Fourier transform is used to decompose an incident Gaussian beam into a continuous spectrum of uniform plane waves (UPWs) propagating in different directions. The scattered fields of each UPW in the spectrum are computed by using the Lorenz-Mie theory. The scattered fields contributed by all the UPWs in the spectrum are superposed to form the total scattered fields. The Maxwell stress tensor derived from the total fields is then used to compute the force density exterior to the particle surface and the time-average net radiation force on the particle.

Typical scenarios for applying radiation force are simulated to study the force exerted by an incident Gaussian beam on spherical particles of different sizes. This is the first article to integrate Fourier transform, Lorenz-Mie theory and Maxwell stress tensor for computing the radiation force exerted by a Gaussian beam on a spherical particle, with rigorous formulations of electromagnetic fields, force density and net force. This is also the first article to systematically compare the distributions of fields and radiation force density. The proposed approach can be extended to Rayleigh scattering and ray-optics regimes.

The rest of this article is organized as follows. The proposed FT-LMT-MST approach is presented in Section II, the simulation results are discussed in Section III, with the contributions and novelties of this work highlighted at the end. Finally, some conclusions are drawn in Section IV.

## II. FORMULATIONS

### A. Field Decomposition of Gaussian Beam

The electric and magnetic fields of an incident Gaussian beam can be decomposed into a continuous spectrum of uniform plane waves (UPWs) propagating in different directions, with their amplitudes determined by using Fourier transform. When each uniform plane wave is incident upon a spherical particle, scattered fields will be induced and determined with the Lorenz-Mie theory (LMT). The total fields exterior to the spherical particle are the superposition of all the constituent incident fields and their scattered fields.

The electric field of a Gaussian beam propagating in  $z$  direction is given by [18]

$$\begin{aligned} \bar{E}_i(\bar{r}) = \hat{x}E_{ix}(\bar{r}) = -\hat{x}j\omega E_a \frac{\sqrt{2}}{\sqrt{\pi}w(z)} e^{j\phi(z)} e^{-jkz} \\ \exp\left\{-\frac{x^2+y^2}{w^2(z)}\right\} \exp\left\{-\frac{jk(x^2+y^2)}{2R_g(z)}\right\} \end{aligned}$$

in the far-field region, where  $\bar{r} = \hat{x}x + \hat{y}y + \hat{z}z$ ,  $w(z) = w_0 \sqrt{1 + \left(\frac{\lambda z}{\pi w_0^2}\right)^2}$  is the beam waist,  $R_g(z) = \frac{z^2 + (\pi w_0^2/\lambda)^2}{z}$  is the radius of curvature of phase front,  $\phi(z) = \tan^{-1} \frac{\lambda z}{\pi w_0^2}$  is the Gouy phase, and  $w_0$  is the waist of Gaussian beam at  $z = 0$ . The associated magnetic field is given by

$$\bar{H}_i(\bar{r}) = \hat{y}H_{iy}(\bar{r}) = \hat{y} \frac{E_{ix}(\bar{r})}{\eta_2}$$

where  $\eta_2$  is the intrinsic impedance of the background medium.

The time-average Poynting vector at  $z = 0$  is

$$\langle \bar{S}(\bar{r}_s, t) \rangle = \frac{1}{2} \text{Re}\{\bar{E}_i(\bar{r}_s) \times \bar{H}_i^*(\bar{r}_s)\} = \hat{z} \frac{\omega^2 |E_a|^2}{\pi w_0^2 \eta_2} e^{-2\rho^2/w_0^2}$$

where  $\bar{r}_s = \hat{x}x + \hat{y}y$ ,  $\rho^2 = x^2 + y^2$ , and the time-average power at  $z = 0$  is computed as

$$\langle P_0 \rangle = \int_0^\infty \int_0^{2\pi} \langle \bar{S}(\bar{r}_s, t) \rangle \cdot \hat{z} \rho d\rho d\phi = \frac{\omega^2 |E_a|^2}{2\eta_2}$$

leading to  $|E_a| = \frac{\sqrt{2\langle P_0 \rangle \eta_2}}{\omega}$ .

At  $z = z_0 = kw_0^2/2$ , a threshold distance of the far-field region [19], the incident electric field  $E_{ix}(\bar{r})$  can be represented in a two-dimensional Fourier transform as

$$\begin{aligned} E_{ix}(\bar{r}) &= E_{i0} e^{-(x^2+y^2)/\ell^2} \\ &= \frac{1}{4\pi^2} \int_{-\infty}^\infty \int_{-\infty}^\infty E_i(k_x, k_y) e^{-j(k_x x + k_y y)} dk_x dk_y \quad (1) \end{aligned}$$

with

$$\begin{aligned} \ell &= \frac{1}{\sqrt{\frac{1}{w^2(z_0)} + \frac{jk}{2R_g(z_0)}}} \\ E_{i0} &= -j\omega E_a \frac{\sqrt{2}}{\sqrt{\pi}w(z_0)} e^{j\phi(z_0)} e^{-jkz_0} \end{aligned}$$

where  $E_i(k_x, k_y)$  is the amplitude of constituent uniform plane wave,  $e^{-j[k_x x + k_y y + k_z(z-z_0)]}$ , and is the inverse Fourier transform of  $E_{ix}(\bar{r})$  in (1) as

$$\begin{aligned} E_i(k_x, k_y) &= \int_{-\infty}^\infty \int_{-\infty}^\infty E_{i0} e^{-(x^2+y^2)/\ell^2} e^{j(k_x x + k_y y)} dx dy \\ &= \pi\alpha^2 E_{i0} e^{-(k_x^2 + k_y^2)\ell^2/4} \end{aligned}$$

The integral in (1) is implemented on a 2D grid in the  $k_x k_y$  plane, with

$$\begin{aligned} k_{wx} &= k \sin \theta_w \cos \phi_w, \quad k_{wy} = k \sin \theta_w \sin \phi_w, \\ 0 &\leq \theta_w \leq \theta_b, \quad 0 \leq \phi_w < 2\pi \end{aligned}$$

where  $\theta_b = \lambda/(\pi n w_0)$  is the diffraction angle of the Gaussian beam with waist  $w_0$  in the medium with refractive index  $n$  [18], and  $k_{wz} = \sqrt{k^2 - k_{wx}^2 - k_{wy}^2}$  is determined by the dispersion relation of uniform plane wave. Thus, the electric field  $E_{ix}(\bar{r})$  in (1), at  $z \geq z_0$ , is approximated as

$$\begin{aligned} E_{ix}(\bar{r}) &\simeq \frac{\Delta k_x \Delta k_y}{4\pi^2} \sum_{\alpha=-N_x/2}^{N_x/2-1} \sum_{\beta=-N_y/2}^{N_y/2-1} E_i(k_{wx}, k_{wy}) \\ &\quad \times e^{-j(k_{wx}x + k_{wy}y + k_{wz}z_p)}, \quad z_p \geq 0 \end{aligned}$$

where  $z_p = z - z_0$ ,  $k_{wx} = \alpha \Delta k_x$ ,  $k_{wy} = \beta \Delta k_y$ ,  $\Delta k_x = B_{kx}/N_x$ ,  $\Delta k_y = B_{ky}/N_y$ ,  $B_{kx}$  and  $B_{ky}$  are the effective bandwidths of  $k_x$  and  $k_y$ , respectively.

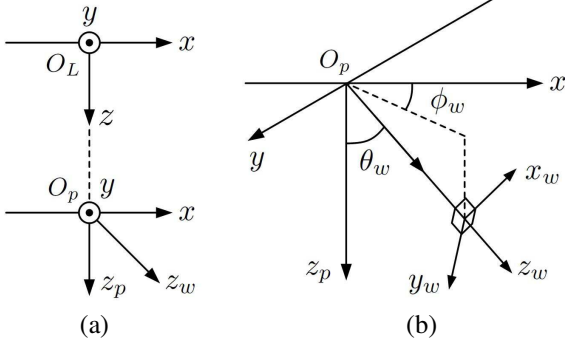


Fig. 1. Schematic of laser coordinate (origin at  $O_L$ ), particle coordinate (origin at  $O_p$ ), and wave coordinate ( $x_w, y_w, z_w$ ).

Fig.1(a) shows the particle coordinate ( $x, y, z_p$ ), with origin at  $O_p = (0, 0, z_0)_L$ , where the subscript  $L$  indicates the laser coordinate ( $x, y, z$ ), with origin at  $O_L = (0, 0, 0)_L$ . Each set of  $(k_{wx}, k_{wy}, k_{wz})$  represents a uniform plane wave propagating in the direction of  $\Omega_w = (\theta_w, \phi_w)$ , where  $\theta_w$  and  $\phi_w$  are the zenith angle and azimuth angle, respectively, of the propagation direction with respect to  $\overline{O_L O_p}$ . A wave coordinate ( $x_w, y_w, z_w$ ) is defined in Fig.1(b), with origin at  $O_p$  and  $z_w$  pointing in the direction  $\Omega_w$ , with

$$\begin{aligned} \hat{z}_w &= \hat{x} \sin \theta_w \cos \phi_w + \hat{y} \sin \theta_w \sin \phi_w + \hat{z} \cos \theta_w \\ \hat{x}_w &= \frac{\hat{x} \cos \theta_w - \hat{z} \sin \theta_w \cos \phi_w}{\sqrt{\cos^2 \theta_w + \sin^2 \theta_w \cos^2 \phi_w}} \\ \hat{y}_w &= \frac{-\hat{x} \sin^2 \theta_w \sin \phi_w \cos \phi_w}{\sqrt{\cos^2 \theta_w + \sin^2 \theta_w \cos^2 \phi_w}} \\ &\quad + \frac{\hat{y}(\cos^2 \theta_w + \sin^2 \theta_w \cos^2 \phi_w) - \hat{z} \sin \theta_w \cos \theta_w \sin \phi_w}{\sqrt{\cos^2 \theta_w + \sin^2 \theta_w \cos^2 \phi_w}} \end{aligned}$$

where  $\hat{x}_w \cdot \hat{y}_w = 0$  and  $\hat{y}_w = \hat{z}_w \times \hat{x}_w$ .

To compute the fields at position  $\vec{r} = \hat{x}x + \hat{y}y + \hat{z}z_p$  when a plane wave is incident in direction  $\Omega_w$ , first transform the coordinates  $(x, y, z_p)$  to  $(x_w, y_w, z_w)$  as

$$x_w = \hat{x}_w \cdot \vec{r}, \quad y_w = \hat{y}_w \cdot \vec{r}, \quad z_w = \hat{z}_w \cdot \vec{r}$$

which are mapped to the spherical coordinates  $(r_m, \theta_m, \phi_m)$  as

$$r_m = \sqrt{x_w^2 + y_w^2 + z_w^2}, \quad \theta_m = \arccos \frac{z_w}{r_m}, \quad \phi_m = \arctan \frac{y_w}{x_w}$$

By Lorenz-Mie theory, the incident fields  $(\bar{E}_{wi}, \bar{H}_{wi})$  and the scattered fields  $(\bar{E}_{ws}, \bar{H}_{ws})$  are given by [8]

$$\bar{E}_{wi} = E_0 \sum_{n=0}^{\infty} (-j)^n \frac{2n+1}{n(n+1)} \left( \bar{M}_{n1,o}^{(2\cap)} + j \bar{N}_{n1,e}^{(2\cap)} \right) \quad (2)$$

$$\bar{H}_{wi} = -\frac{E_0}{\eta_2} \sum_{n=0}^{\infty} (-j)^n \frac{2n+1}{n(n+1)} \left( \bar{M}_{n1,e}^{(2\cap)} - j \bar{N}_{n1,o}^{(2\cap)} \right) \quad (3)$$

$$\bar{E}_{ws} = E_0 \sum_{n=0}^{\infty} (-j)^n \frac{2n+1}{n(n+1)} \left( A_n \bar{M}_{n1,o}^{(2\cup)} + j B_n \bar{N}_{n1,e}^{(2\cup)} \right) \quad (4)$$

$$\bar{H}_{ws} = -\frac{E_0}{\eta_2} \sum_{n=0}^{\infty} (-j)^n \frac{2n+1}{n(n+1)} \left( B_n \bar{M}_{n1,e}^{(2\cup)} - j A_n \bar{N}_{n1,o}^{(2\cup)} \right) \quad (5)$$

where  $E_0 = \Delta k_x \Delta k_y E_i(k_{wx}, k_{wy}) / (4\pi^2)$ , and the components of vector spherical harmonics are

$$\begin{aligned} M_{nm,r} &= 0 \\ M_{nm,\theta} &= \frac{m}{\sin \theta} z_n(kr) P_n^m(\cos \theta) \begin{cases} -\sin(m\phi) \\ \cos(m\phi) \end{cases} \\ M_{nm,\phi} &= -z_n(kr) \frac{\partial P_n^m(\cos \theta)}{\partial \theta} \begin{cases} \cos(m\phi) \\ \sin(m\phi) \end{cases} \\ N_{nm,r} &= \frac{n(n+1)}{kr} z_n(kr) P_n^m(\cos \theta) \begin{cases} \cos(m\phi) \\ \sin(m\phi) \end{cases} \\ N_{nm,\theta} &= \frac{1}{kr} \frac{\partial(r z_n(kr))}{\partial r} \frac{\partial P_n^m(\cos \theta)}{\partial \theta} \begin{cases} \cos(m\phi) \\ \sin(m\phi) \end{cases} \\ N_{nm,\phi} &= \frac{m}{kr \sin \theta} \frac{\partial(r z_n(kr))}{\partial r} P_n^m(\cos \theta) \begin{cases} -\sin(m\phi) \\ \cos(m\phi) \end{cases} \end{aligned} \quad (6)$$

where the azimuthal functions at top and bottom are used for even modes and odd modes, respectively,  $z_n(kr)$  is the spherical Bessel function, and  $P_n^m(\cos \theta)$  is the associated Legendre polynomial. The permeability and permittivity of the background medium are  $(\mu_2, \epsilon_2)$ ,  $k_2 = \omega \sqrt{\mu_2 \epsilon_2}$ ,  $\eta_2 = \sqrt{\mu_2 / \epsilon_2}$ . The superscript  $(2\cap)$  indicates  $z_n(kr) = j_n(k_2 r)$ , and  $(2\cup)$  indicates  $z_n(kr) = h_n^{(2)}(k_2 r)$ . The coefficients in (4), (5) are given by [8]

$$A_n = \frac{\mu_2 \zeta_{\cap 2} \xi_1 - \mu_1 \zeta_1 \xi_{\cap 2}}{\mu_1 \zeta_1 \xi_{\cup 2} - \mu_2 \zeta_{\cup 2} \xi_1}, \quad B_n = \frac{\mu_2 N_{12}^2 \zeta_1 \xi_{\cap 2} - \mu_1 \zeta_{\cap 2} \xi_1}{\mu_1 \zeta_{\cup 2} \xi_1 - \mu_2 N_{12}^2 \zeta_1 \xi_{\cup 2}}$$

where

$$\begin{aligned} \zeta_{\cap 2} &= j_n(k_2 a), \quad \zeta_1 = j_n(k_1 a), \quad \zeta_{\cup 2} = h_n^{(2)}(k_2 a) \\ \xi_{\cap 2} &= \left. \frac{\partial r j_n(k_2 r)}{\partial r} \right|_{r=a}, \quad \xi_1 = \left. \frac{\partial r j_n(k_1 r)}{\partial r} \right|_{r=a}, \\ \xi_{\cup 2} &= \left. \frac{\partial r h_n^{(2)}(k_2 r)}{\partial r} \right|_{r=a} \end{aligned}$$

The incident and scattered fields associated with the incident plane wave propagating in direction  $\Omega_w$  are then mapped to the  $(x, y, z_p)$  coordinates to have

$$\begin{aligned} \bar{E}_{pi}(\Omega_w) &= \hat{x}(\hat{x} \cdot \bar{E}_{wi}) + \hat{y}(\hat{y} \cdot \bar{E}_{wi}) + \hat{z}(\hat{z} \cdot \bar{E}_{wi}) \\ \bar{H}_{pi}(\Omega_w) &= \hat{x}(\hat{x} \cdot \bar{H}_{wi}) + \hat{y}(\hat{y} \cdot \bar{H}_{wi}) + \hat{z}(\hat{z} \cdot \bar{H}_{wi}) \\ \bar{E}_{ps}(\Omega_w) &= \hat{x}(\hat{x} \cdot \bar{E}_{ws}) + \hat{y}(\hat{y} \cdot \bar{E}_{ws}) + \hat{z}(\hat{z} \cdot \bar{E}_{ws}) \\ \bar{H}_{ps}(\Omega_w) &= \hat{x}(\hat{x} \cdot \bar{H}_{ws}) + \hat{y}(\hat{y} \cdot \bar{H}_{ws}) + \hat{z}(\hat{z} \cdot \bar{H}_{ws}) \end{aligned}$$

The incident and scattered fields of the whole Gaussian beam are the sum of their constituent components over all  $\Omega_w$ 's as

$$\begin{aligned} \bar{E}_{pi} &= \sum_{\Omega_w} \bar{E}_{pi}(\Omega_w), \quad \bar{H}_{pi} = \sum_{\Omega_w} \bar{H}_{pi}(\Omega_w), \\ \bar{E}_{ps} &= \sum_{\Omega_w} \bar{E}_{ps}(\Omega_w), \quad \bar{H}_{ps} = \sum_{\Omega_w} \bar{H}_{ps}(\Omega_w) \end{aligned}$$

### B. Maxwell Stress Tensor and Time-Average Radiation Force

The Maxwell stress tensor is given by [9]

$$\bar{\mathbf{T}}(\bar{\mathbf{r}}, t) = \epsilon \bar{\mathbf{E}} \bar{\mathbf{E}} + \mu \bar{\mathbf{H}} \bar{\mathbf{H}} - \frac{1}{2} \bar{\mathbf{I}}(\epsilon E^2 + \mu H^2)$$

and the radiation force density (Nt/m<sup>2</sup>) on a spherical surface in region (2) is derived as

$$\begin{aligned} \bar{\mathbf{F}}(\bar{\mathbf{r}}, t) &= \bar{\mathbf{T}}(\bar{\mathbf{r}}, t) \cdot \hat{\mathbf{n}} \\ &= \left[ \epsilon_2 \bar{\mathbf{E}}_2 \bar{\mathbf{E}}_2 + \mu_2 \bar{\mathbf{H}}_2 \bar{\mathbf{H}}_2 - \frac{1}{2} \bar{\mathbf{I}}(\epsilon_2 E_2^2 + \mu_2 H_2^2) \right] \cdot \hat{\mathbf{r}} \end{aligned}$$

where  $\bar{\mathbf{I}}$  is an identity dyadic,  $\bar{\mathbf{E}}_2(\bar{\mathbf{r}}, t) = \bar{\mathbf{E}}_{pi}(\bar{\mathbf{r}}, t) + \bar{\mathbf{E}}_{ps}(\bar{\mathbf{r}}, t)$  is the total electric field,  $\bar{\mathbf{H}}_2(\bar{\mathbf{r}}, t) = \bar{\mathbf{H}}_{pi}(\bar{\mathbf{r}}, t) + \bar{\mathbf{H}}_{ps}(\bar{\mathbf{r}}, t)$  is the total magnetic field, and

$$\begin{aligned} E_2^2(\bar{\mathbf{r}}, t) &= E_{2r}^2(\bar{\mathbf{r}}, t) + E_{2\theta}^2(\bar{\mathbf{r}}, t) + E_{2\phi}^2(\bar{\mathbf{r}}, t) \\ H_2^2(\bar{\mathbf{r}}, t) &= H_{2r}^2(\bar{\mathbf{r}}, t) + H_{2\theta}^2(\bar{\mathbf{r}}, t) + H_{2\phi}^2(\bar{\mathbf{r}}, t) \end{aligned}$$

The radiation force can be derived from the Maxwell stress tensor on a spherical surface that encloses the spherical particle, with outward unit normal vector  $\hat{\mathbf{n}} = \hat{\mathbf{r}}$  [9], [14]. The time-average force density can then be derived as

$$\begin{aligned} \langle \bar{\mathbf{F}}(\bar{\mathbf{r}}, t) \rangle &= \frac{1}{2} \text{Re} \left\{ \left[ \epsilon_2 \bar{\mathbf{E}}_2(\bar{\mathbf{r}}) \bar{\mathbf{E}}_2^*(\bar{\mathbf{r}}) + \mu_2 \bar{\mathbf{H}}_2(\bar{\mathbf{r}}) \bar{\mathbf{H}}_2^*(\bar{\mathbf{r}}) \right. \right. \\ &\quad \left. \left. - \frac{1}{2} \bar{\mathbf{I}}(\epsilon_2 E_2^2(\bar{\mathbf{r}}) + \mu_2 H_2^2(\bar{\mathbf{r}})) \right] \cdot \hat{\mathbf{r}} \right\} \\ &= \hat{\mathbf{r}} \langle F_r(\bar{\mathbf{r}}, t) \rangle + \hat{\theta} \langle F_\theta(\bar{\mathbf{r}}, t) \rangle + \hat{\phi} \langle F_\phi(\bar{\mathbf{r}}, t) \rangle \\ &= \hat{x} \langle F_x(\bar{\mathbf{r}}, t) \rangle + \hat{y} \langle F_y(\bar{\mathbf{r}}, t) \rangle + \hat{z} \langle F_z(\bar{\mathbf{r}}, t) \rangle \end{aligned}$$

where the Cartesian and the spherical components are related as

$$\begin{aligned} \langle F_x(\bar{\mathbf{r}}, t) \rangle &= \sin \theta \cos \phi \langle F_r(\bar{\mathbf{r}}, t) \rangle \\ &\quad + \cos \theta \cos \phi \langle F_\theta(\bar{\mathbf{r}}, t) \rangle - \sin \phi \langle F_\phi(\bar{\mathbf{r}}, t) \rangle \\ \langle F_y(\bar{\mathbf{r}}, t) \rangle &= \sin \theta \sin \phi \langle F_r(\bar{\mathbf{r}}, t) \rangle \\ &\quad + \cos \theta \sin \phi \langle F_\theta(\bar{\mathbf{r}}, t) \rangle + \cos \phi \langle F_\phi(\bar{\mathbf{r}}, t) \rangle \\ \langle F_z(\bar{\mathbf{r}}, t) \rangle &= \cos \theta \langle F_r(\bar{\mathbf{r}}, t) \rangle - \sin \theta \langle F_\theta(\bar{\mathbf{r}}, t) \rangle \end{aligned}$$

The time-average radiation force in the axial direction of the Gaussian beam is computed as

$$\langle f_z(t) \rangle = \int_0^{2\pi} \int_0^\pi \langle F_z(\bar{\mathbf{r}}, t) \rangle R^2 \sin \theta d\theta d\phi$$

where  $R$  is the radius of spherical surface enclosing the particle.

### III. SIMULATIONS AND DISCUSSIONS

TABLE I  
DEFAULT PARAMETERS USED IN SIMULATIONS.

parameter	symbol	value	ref.
laser wavelength	$\lambda$	1,064 nm	[20], [21]
laser power	$P_0$	50 mW	[22]
particle material		polystyrene	[20], [23]
particle refractive index	$n_1$	1.5694	[24]
particle radius	$a$	1.03 $\mu\text{m}$	[20]
background medium		water	[20], [25]
background refractive index	$n_2$	1.3239	[24]

Table 1 lists the default parameters used in the simulations. In [20], polystyrene ( $\text{C}_8\text{H}_8$ )<sub>n</sub> particles of radius  $a = 1.03 \mu\text{m}$

were suspended in water for experiment, with laser wavelength of 1,064 nm and laser power of 2.3-9.2 mW. Polystyrene particles were used as the beads for optical trapping and steering of biological cells such as red blood cells (RBCs) [23]. Aqueous suspension was commonly used for studying RBC magnetophoresis [25]. At temperature  $T = 20^\circ\text{C}$ , the refractive index of water ( $\text{H}_2\text{O}$ ) is  $n = 1.3239$  [24], and that of polystyrene is  $n = 1.5694$  [24]. The dielectric constant of a non-magnetic material is related to its refractive index as  $\epsilon_r = n^2$ .

In [21], an optical tweezer was used to study the deformation of human red blood cells, in which a Nd:YAG laser source at wavelength of 1,064 nm was used. The maximum power of Nd:YAG laser was 1.5 W, and could be adjusted between 2 and 80 mW [22].

In this work, a Nd:YAG laser with power of  $P_0 = 50$  mW at wavelength  $\lambda = 1,064$  nm is adopted in the simulations, exerting force on a spherical polystyrene particle immersed in the water. We will first study the effect of particle radius on electric field and radiation force density. A Gaussian beam of waist  $w_0 = 100\lambda$  is assumed. The distributions of electric field components ( $E_x$ ,  $E_y$ ,  $E_z$ ) and time-average force densities ( $\langle F_x \rangle$ ,  $\langle F_y \rangle$ ,  $\langle F_z \rangle$ ) will be presented and discussed.

#### A. Electric Field and Radiation Force Density Near Particle Surface

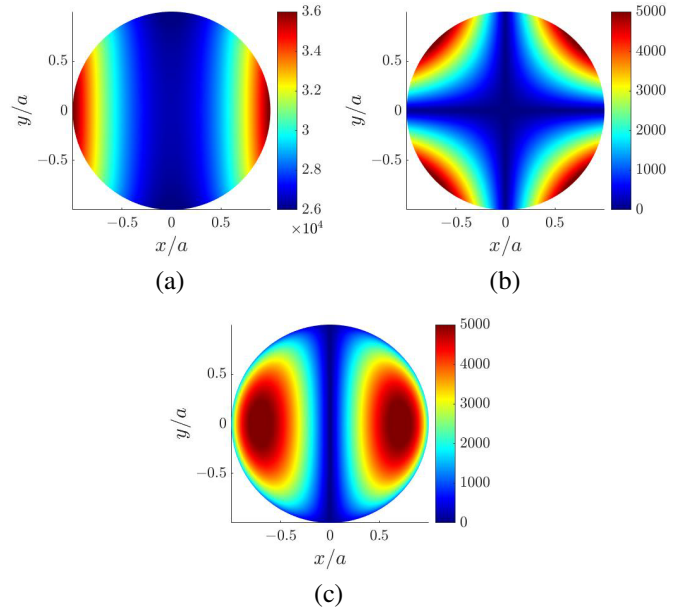


Fig. 2. Magnitude of electric field on northern hemisphere projected onto  $xy$  plane,  $a = 0.1 \mu\text{m}$ ,  $k_2 a = 0.7818$ ,  $R = 1.01a$ ,  $w_0 = 100\lambda$ ,  $31 \times 31$  UPWs, (a)  $|E_x(\bar{\mathbf{r}})|$ , (b)  $|E_y(\bar{\mathbf{r}})|$ , (c)  $|E_z(\bar{\mathbf{r}})|$ .

Figs.2(a)-2(c) show the magnitude of electric field components on the northern hemisphere of a surface with radius  $R = 1.01a$ , projected onto  $xy$  plane. The incident Gaussian beam has a minimum beam radius of  $w_0 = 100\lambda$ , and is decomposed into  $31 \times 31$  UPWs. The incident electric field is  $x$ -polarized, and the scattered field component  $|E_x|$ , as shown in Fig.2(a), is much stronger than the other two components shown in Figs.2(b) and 2(c). Note that the magnitude of

dominant scattered field component  $|E_x|$  undulates by about 30 % of the maximum value, compatible to the feature of uniform field distribution within a small particle in the Rayleigh scattering regime.

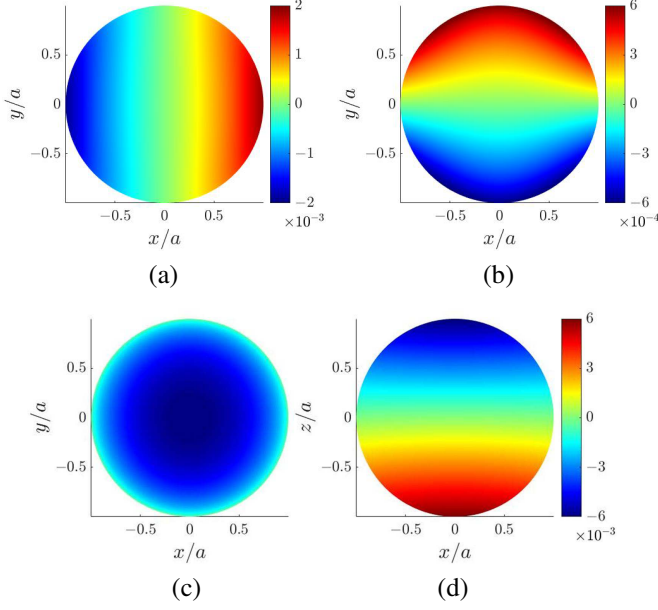


Fig. 3. Time-average force density on northern hemisphere projected onto  $xy$  plane,  $a = 0.1\mu\text{m}$ ,  $k_2a = 0.7818$ ,  $R = 1.01a$ ,  $w_0 = 100\lambda$ ,  $31 \times 31$  UPWs, (a)  $\langle F_x(\bar{r}, t) \rangle$ , (b)  $\langle F_y(\bar{r}, t) \rangle$ , (c)  $\langle F_z(\bar{r}, t) \rangle$ . (d) Projection of  $\langle F_z(\bar{r}, t) \rangle$  onto  $xz$  plane.

Figs.3(a)-3(c) show the force density distributions on the northern hemisphere, projected onto  $xy$  plane. Figs.3(a) and 3(b) show the force density distributions of  $\langle F_x(\bar{r}, t) \rangle$  and  $\langle F_y(\bar{r}, t) \rangle$ , respectively, leading to zero net force in  $x$  and  $y$  directions by symmetry.

Fig.3(c) shows the distribution of force density  $\langle F_z(\bar{r}, t) \rangle$  on the northern hemisphere, which appears to be negative and insensitive to azimuthal angle. Fig.3(d) shows the distribution of  $\langle F_z(\bar{r}, t) \rangle$  projected onto the  $xz$  plane, manifesting negative value on the northern hemisphere and positive value on the southern hemisphere. The patterns on both hemispheres look similar and their magnitudes are comparable. The net force in the  $z$  direction turns out to be positive, which will be illustrated later.

Figs.4(a)-4(c) show the magnitude of electric field components with  $a = 1.03\mu\text{m}$ , about ten times larger than that in Fig.2, and the other parameters are the same. Standing-wave like patterns emerge, as compared with the more uniform patterns in the previous case.

Figs.5(a)-5(c) show the time-average force density distributions on the particle with radius  $a = 1.03\mu\text{m}$ . The distributions of  $\langle F_x(\bar{r}, t) \rangle$  and  $\langle F_y(\bar{r}, t) \rangle$  manifest similar standing-wave like features as in Fig.4. The force density is more concentrated around the  $z$ -axis as compared with that in Fig.3. Fig.5(c) shows strong negative force density in circular pattern around the  $z$  axis, which suggests the incident beam mainly impacts the central surface of the particle when the particle radius is about one wavelength.

Figs.6(a)-6(c) show the distributions of electric field components on the northern hemisphere, with particle radius

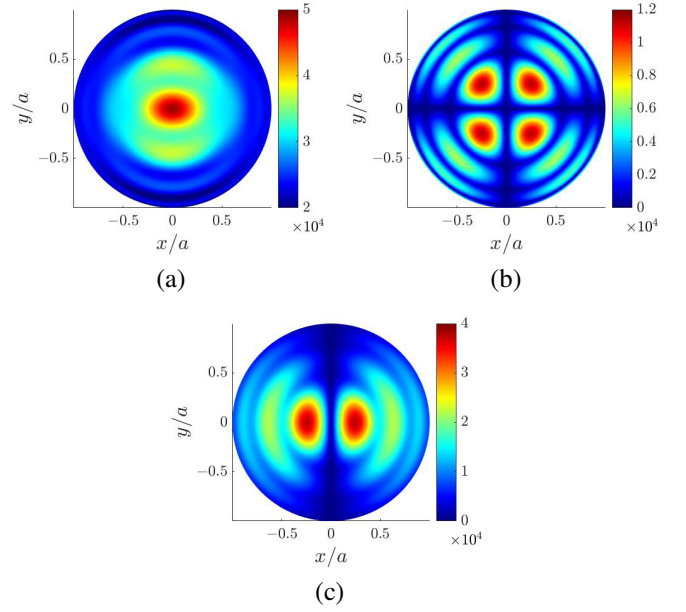


Fig. 4. Magnitude of electric field on northern hemisphere projected onto  $xy$  plane,  $a = 1.03\mu\text{m}$ ,  $k_2a = 8.0525$ ,  $R = 1.01a$ ,  $w_0 = 100\lambda$ ,  $31 \times 31$  UPWs, (a)  $|E_x(\bar{r})|$ , (b)  $|E_y(\bar{r})|$ , (c)  $|E_z(\bar{r})|$ .

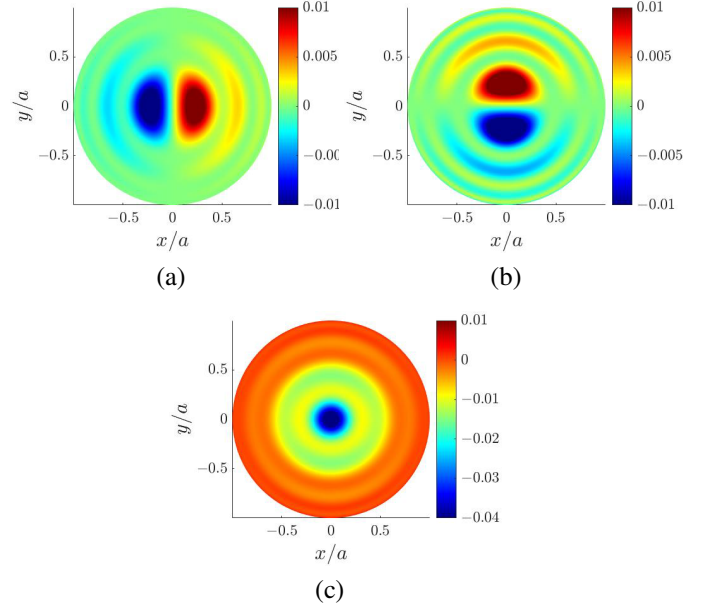


Fig. 5. Time-average force density on northern hemisphere projected onto  $xy$  plane,  $a = 1.03\mu\text{m}$ ,  $k_2a = 8.0525$ ,  $R = 1.01a$ ,  $w_0 = 100\lambda$ ,  $31 \times 31$  UPWs, (a)  $\langle F_x(\bar{r}, t) \rangle$ , (b)  $\langle F_y(\bar{r}, t) \rangle$ , (c)  $\langle F_z(\bar{r}, t) \rangle$ .

$a = 2.5\mu\text{m}$  and the other parameters are the same. Compared with Figs.2 and 4, the field patterns manifest more undulation across the hemisphere and concentrate closer to the  $z$  axis as the particle size increases.

Fig.7 shows the time-average force density distribution with  $a = 2.5\mu\text{m}$ . It is observed that  $\langle F_x(\bar{r}, t) \rangle$  in Fig.7(a) is antisymmetric about  $y$  axis and  $\langle F_y(\bar{r}, t) \rangle$  in Fig.7(b) is antisymmetric about  $x$  axis. More fringe stripes are counted across the diameter than in the previous two cases. Fig.7(c) shows the distribution of  $\langle F_z(\bar{r}, t) \rangle$  is radially symmetric about the  $z$ -axis, and is more concentrated around the  $z$  axis than in



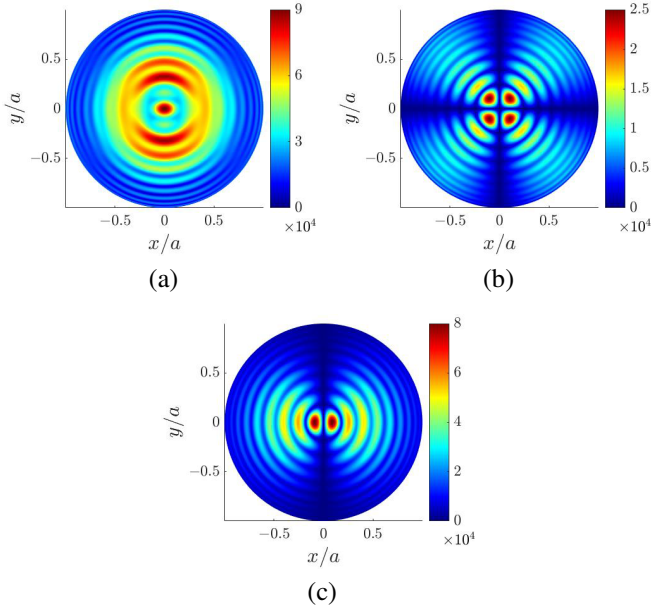


Fig. 6. Magnitude of electric field on northern hemisphere projected onto  $xy$  plane,  $a = 2.5\mu\text{m}$ ,  $k_2a = 19.5449$ ,  $R = 1.01a$ ,  $w_0 = 100\lambda$ ,  $31 \times 31$  UPWs, (a)  $|E_x(\vec{r})|$ , (b)  $|E_y(\vec{r})|$ , (c)  $|E_z(\vec{r})|$ .

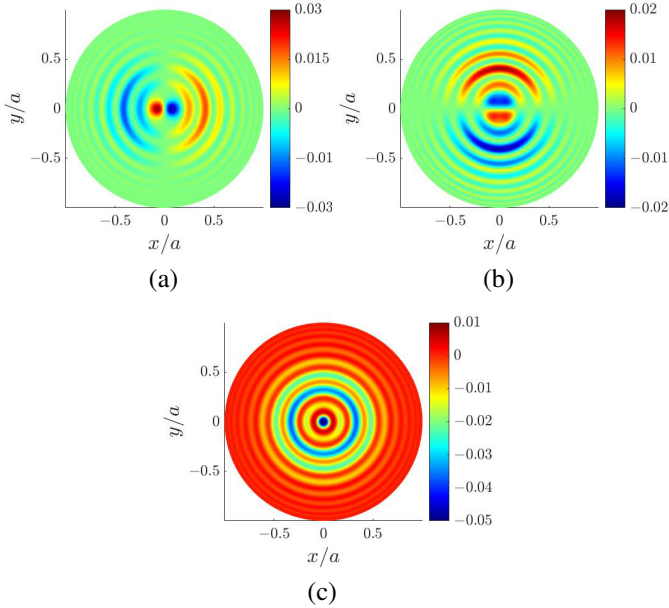


Fig. 7. Time-average force density on northern hemisphere projected onto  $xy$  plane,  $a = 2.5\mu\text{m}$ ,  $k_2a = 19.5449$ ,  $R = 1.01a$ ,  $w_0 = 100\lambda$ ,  $31 \times 31$  UPWs, (a)  $\langle F_x(\vec{r}, t) \rangle$ , (b)  $\langle F_y(\vec{r}, t) \rangle$ , (c)  $\langle F_z(\vec{r}, t) \rangle$ .

the previous two cases.

Note that Figs.6(a) and 7(c) manifest the strongest electric field and radiation force density, respectively, around the  $z$ -axis, as if the incident beam directly impacts the polar regions of the particle, which is consistent with the prediction in the ray-optics regime.

Comparing Figs.3(c), 5(c) and 7(c), it is found that the negative force density increases in magnitude and decreases in area when the particle becomes larger. One may use the terminology of ray-optics to understand this phenomenon [26]. The net force exerted on a particle is the force generated by

the incident ray deducting the force generated by the scattering rays. In this work, the incident ray hits the particle at  $z_p = -a$ . Part of the ray is reflected and part of it is transmitted into the particle. The latter part propagates through the particle and hits the particle boundary at  $z_p = a$ . Part of this ray is reflected and part of it is transmitted into the background medium. The ray leaving the particle at  $z_p = a$  generates negative force density by reaction. Note that this explanation is more applicable to large particle ( $k_2a$  is large).

Next, we will present the time-average radiation force  $\langle f_z(t) \rangle$  versus  $k_2a$ , with Gaussian beams of different  $w_0$ 's. The results of uniform plane wave is also presented for comparison.

### B. Oscillation Phenomenon on Radiation Force

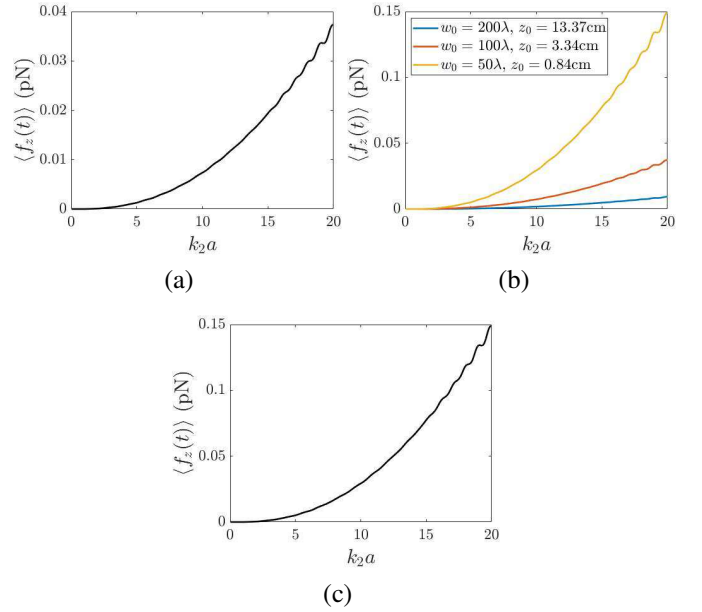


Fig. 8. Time-average radiation force  $\langle f_z(t) \rangle$  versus  $k_2a$ , with  $R = 1.01a$ ,  $n_1 = 1.5694$ ,  $n_2 = 1.3239$ , (a) UPW, (b) GBs in three scenarios, (c) calibration of (b) with (7).

Fig.8(a) shows the time-average radiation force  $\langle f_z(t) \rangle$  versus  $k_2a$ , exerted by an incident uniform plane wave with magnitude of electric field

$$|E_0| = \frac{\sqrt{2\langle P_0 \rangle \eta}}{\pi w_0^2}$$

where  $w_0 = 100\lambda$  is an effective beam waist for the convenience of estimating the magnitude of electric field from the given laser power. Figs.8(a) and 8(b) show that aside from the magnitude difference between the curves, the time-average radiation force  $\langle f_z(t) \rangle$  increases with  $k_2a$  for both UPW and GB in different scenarios.

Fig.8(b) shows  $\langle f_z(t) \rangle$  versus  $k_2a$  in three different scenarios with incident Gaussian beam. The blue curve ( $\langle f_{z1}(t) \rangle$ ) is computed at  $z_0 = k_2 w_0^2 / 2 = 13.37$  cm with  $w_0 = 200\lambda$ , the orange curve ( $\langle f_{z2}(t) \rangle$ ) is computed at  $z_0 = 3.34$  cm with  $w_0 = 100\lambda$ , and the yellow curve ( $\langle f_{z3}(t) \rangle$ ) is computed at  $z_0 = 0.84$  cm with  $w_0 = 50\lambda$ . The three curves manifest similar trends. By taking a closer look, we find the relation

$$4^2 \langle f_{z1}(t) \rangle = 2^2 \langle f_{z2}(t) \rangle = \langle f_{z3}(t) \rangle \quad (7)$$

which is verified in Fig.8(c) that these three curves overlap after calibration with (7). In other words, if a particle is placed at the far-field threshold  $z_0 = k_2 w_0^2/2$ , the time-average force  $\langle f_z(t) \rangle$  is inversely proportional to  $z_0$  or  $w_0^2$ .

The magnitudes of  $\langle f_x(t) \rangle$  and  $\langle f_y(t) \rangle$  are on the level of numerical noise, consistent with the prediction by symmetry.

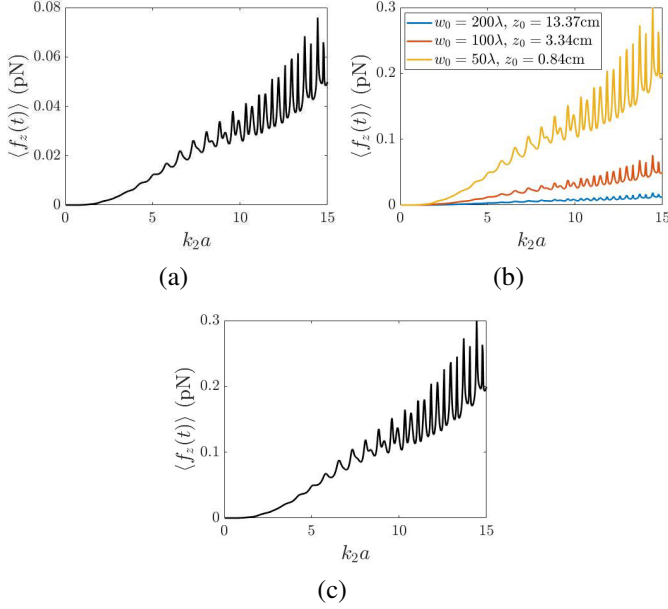


Fig. 9. Time-average radiation force  $\langle f_z(t) \rangle$  versus  $k_2 a$ , with  $n_1 = 1.5$ ,  $n_2 = 1$ , (a) UPW, (b) GBs in three scenarios, (c) calibration of (b) with (7).

The difference between  $n_1$  and  $n_2$  in the previous case is relatively small. Fig.9 shows the counterparts to Fig.8, with  $n_1 = 1.5$  and  $n_2 = 1$ . Oscillation phenomenon is observed in all the curves and becomes more obvious at  $k_2 a > 5$ , with the particle size comparable or larger than one wavelength. Similar oscillation phenomenon was also observed in [9], [14], [27]-[30], referred to as ripple [27], [28], undulation [29], optical resonance [30] or plasmon resonance [14]. A plane wave incident upon a spherical particle is partly reflected multiple times within the dielectric sphere [29], resulting in van de Hulst dielectric surface waves [27], [28], [30]. The surface waves traverse the spherical surface at small diffraction loss [30], and their constructive interference is the cause of oscillation phenomenon.

### C. Highlight of Contributions

- (1) This is the first article to integrate the Fourier transform for decomposing an incident Gaussian beam, the Mie scattering theory for computing the scattered fields, and the Maxwell stress tensor for computing the radiation force exerted on a spherical particle.
- (2) The proposed approach is rigorous, taking no mathematical approximations, in deriving the scattered fields, the radiation force density and the net radiation force of a Gaussian beam on a spherical particle. Thus, the proposed approach can be applied to Rayleigh scattering and ray-optics regime as well.
- (3) This is the first article that presents the distributions of electric field and radiation force density on a spherical

surface enclosing the particle as well as the net time-average radiation force exerted with different Gaussian-beam waists.

- (4) This is the first article to simulate and discuss the oscillation phenomenon in radiation force of an incident Gaussian beam on a spherical particle.

## IV. CONCLUSION

An FT-LMT-MST approach has been developed to compute the radiation force exerted by a Gaussian beam on a spherical particle, by integrating the Fourier transform, the Lorenz-Mie theory and the Maxwell stress tensor. The scattered fields, radiation force density and net force can be derived rigorously and computed numerically. Distributions of electric field and radiation force density have been presented and analyzed systematically. The negative force density on part of the enclosing surface, the comparison with results of an uniform plane wave, and the oscillation phenomenon of radiation force have also been elaborated.

## REFERENCES

- [1] Y. K. Nahmias and D. J. Odde, "Analysis of radiation forces in laser trapping and laser-guided direct writing applications," *IEEE J. Quantum Electron.*, vol. 38, pp. 131-141, Feb. 2002.
- [2] A. Ashkin, "Acceleration and trapping of particles by radiation pressure," *Phys. Rev. Lett.*, vol. 24, pp. 156V159, 1970.
- [3] A. Ashkin and J. M. Dziedzic, "Optical levitation by radiation pressure," *Appl. Phys. Lett.*, vol. 19, pp. 283V285, 1971.
- [4] X. Wang, X. B. Wang, and P. R. C. Gascoyne, "General expressions for dielectrophoretic force and electrorotational torque derived using the Maxwell stress tensor method," *J. Electrostatics*, vol. 39, pp. 277-295, 1997.
- [5] G. Pesce, P. H. Jones, O. M. Maragò, and G. Volpe, "Optical tweezers: Theory and practice," *Euro. Phys. J. Plus*, vol. 135, pp. 949-1-38, 2020.
- [6] C. Zhang, K. Khoshmanesh, A. Mitchell, and K. Kalantar-Zadeh, "Dielectrophoresis for manipulation of micro/nano particles in microfluidic systems," *Anal. Bioanal. Chem.*, vol. 396, pp. 401-420, Jul. 2009.
- [7] G. Fuhr, T. Schnelle, T. Müller, H. Hitzler, S. Monajembashi, and K.-O. Greulich, "Force measurements of optical tweezers in electro-optical cages," *Appl. Phys. A*, vol. 67, pp. 385V390, Oct. 1998.
- [8] J. A. Stratton, *Electromagnetic Theory*, McGraw-Hill, 1941.
- [9] B. A. Kemp, T. M. Grzegorzczak, and J. A. Kong, "Lorentz force on dielectric and magnetic particles," *J. Electromag. Waves Appl.*, vol. 20, pp. 827-839, 2006.
- [10] J. A. Lock and G. Gouesbet, "Rigorous justification of the localized approximation to the beam-shape coefficients in generalized Lorenz-Mie theory. I. On-axis beams," *J. Opt. Soc. Am. A*, vol. 11, pp. 2503-2515, Sep. 1994.
- [11] J. P. Barton, D. R. Alexander, and S. A. Schaub, "Theoretical determination of net radiation force and torque for a spherical particle illuminated by a focused laser beam," *J. Appl. Phys.*, vol. 66, pp. 4594-4602, Nov. 1989.
- [12] G. Gouesbet, B. Maheu, and G. Gréhan, "Light scattering from a sphere arbitrarily located in a Gaussian beam, using a Bromwich formulation," *J. Opt. Soc. Am. A*, vol. 5, pp. 1427-1443, Sep. 1988.
- [13] Q. Ye and H. Lin, "On deriving the Maxwell stress tensor method for calculating the optical force and torque on an object in harmonic electromagnetic fields," *Euro. J. Phys.*, vol. 38, pp. 1-9, May 2017.
- [14] A. Y. Bekshaev, K. Y. Bliokh, and F. Nori, "Mie scattering and optical forces from evanescent fields: A complex-angle approach," *Opt. Express*, vol. 21, pp. 7082-7095, 2013.
- [15] V. V. Datsyuk and O. R. Pavlyniuk, "Maxwell stress on a small dielectric sphere in a dielectric," *Phys. Rev. A*, vol. 91, 023826, Feb. 2015.
- [16] Z.-S. Wu, Q.-K. Yuan, Y. Peng, and Z.-J. Li, "Internal and external electromagnetic fields for on-axis Gaussian beam scattering from a uniaxial anisotropic sphere," *J. Opt. Soc. Am. A*, vol. 26, pp. 1778-1787, Aug. 2009.
- [17] F. M. Dickey and S. C. Holswade, "Gaussian laser beam profile shaping," *Opt. Eng.*, vol. 35, pp. 3285-3295, Nov. 1996.

- [18] H. A. Haus, *Waves and Fields in Optoelectronics*, Englewood Cliffs, NJ: Prentice-Hall, 1984.
- [19] J. W. Goodman, *Introduction to Fourier Optics*, 2nd ed. New York, NY: McGraw-Hill, 1996.
- [20] J. Gieseler *et al.*, “Optical tweezers - From calibration to applications: A tutorial,” *Advances in Optics and Photonics*, vol. 13, pp. 74-241, Mar. 2021.
- [21] M. Dao, C. T. Lim, and S. Suresh, “Mechanics of the human red blood cell deformed by optical tweezers,” *J. Mechanics Phys. Solids*, vol. 51, pp. 2259V2280, 2003.
- [22] N. Malagnino, G. Pesce, A. Sasso, E. Arimondo, “Measurements of trapping efficiency and stiffness in optical tweezers,” *Optics Commun.*, vol. 214, pp. 15-24, 2002.
- [23] M. W. Berns, “Optical tweezers: Tethers, wavelengths, and heat,” *Methods in Cell Biology*, vol. 82, pp. 457-466, 2007.
- [24] Refractive index database, <https://refractiveindex.info/> (accessed Oct. 1, 2022).
- [25] M. Zborowski *et al.*, “Red blood cell magnetophoresis,” *Biophysical J.*, vol. 84, pp. 2638-2645, Apr. 2003.
- [26] A. Callegari, M. Mijalkov, A. B. Gököz, and G. Volpe, “Computational toolbox for optical tweezers in geometrical optics,” *J. Opt. Soc. Am. B*, vol. 32, pp. B11-B19, 2015.
- [27] H. C. van de Hulst, *Light Scattering by Small Particles*, New York, NY: Dover, 1981.
- [28] W. M. Irvine, “Light scattering by spherical particles: Radiation pressure, asymmetry factor, and extinction cross section,” *J. Opt. Soc. Am.*, vol. 55, pp. 16-21, 1965.
- [29] F. G. Mitri, “Radiation force and torque of light-sheets,” *J. Opt.*, vol. 19, 065403, 2017.
- [30] A. Ashkin and J. M. Dziedzic, “Observation of optical resonances of dielectric spheres by light scattering,” *Appl. Opt.*, vol. 20, pp. 1803-1814, 1981.